# Study of Excited $\Xi^-$ Baryons in $\bar{\text{p}}$p-Collisions with $\overline{\text{P}}$ANDA

Authors:

Jennifer Pütz, Albrecht Gillitzer, James Ritman, Tobias Stockmanns

# Contents

# 1 Introduction

Understanding the excitation pattern of baryons is indispensable for a deep insight into the mechanism of non-perturbative QCD. Up to now only the nucleon excitation spectrum has been subject to systematic experimental studies while very little is known on excited states of double or triple strange baryons.

In studies of antiproton-proton collisions the $\overline{\text{P}}$ANDA experiment is well-suited for a comprehensive baryon spectroscopy program in the multi-strange and charm sector. A large fraction of the inelastic $\bar{\text{p}}$p cross section is associated to final states with a baryon-antibaryon pair together with additional mesons, giving access to excited states both in the baryon and the antibaryon sector.

In the present study we focus on excited $\Xi^-$ states. For final states containing a $\Xi^- \bar{\Xi}^+$ pair cross sections up to the order of $\mu$b are expected, corresponding to production rates of $\sim 10^6/\text{d}$ at a Luminosity $L = 10^{31}\,\text{cm}^{-2}\,\text{s}^{-1}$ (5% of the full value). A strategy to study the excitation spectrum of $\Xi^-$ baryons in antiproton-proton collisions will be discussed. The reconstruction of reactions of the type $\bar{\text{p}}\text{p} \to \Xi^{-*}\bar{\Xi}^+$ (and their charge conjugate) with the $\overline{\text{P}}$ANDA detector will be presented based on a selected exemplary reaction and decay channel.

# 2 Event generation

To study excited $\Xi^-$ baryons the simulation of a sufficient number of signal events is needed. For this study 1.5 million signal events were generated with the event generator EvtGen. The reaction and decay tree selected for the simulation is shown in figure 2.1. If not otherwise specified, the charged conjugate process is implicitly included in the following.
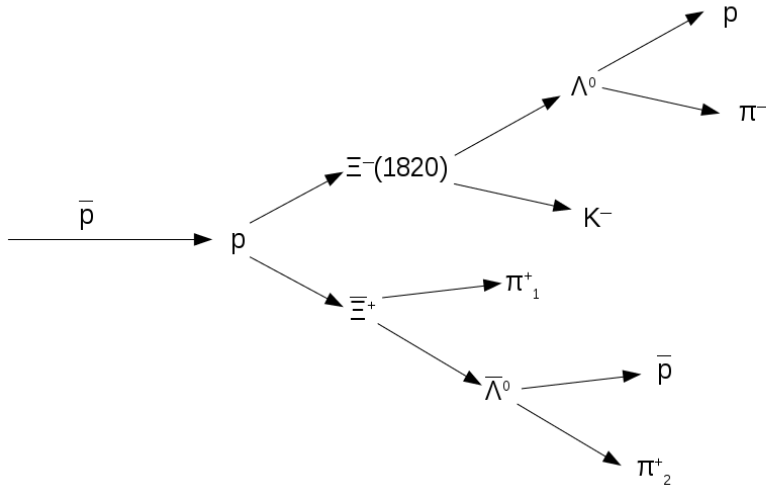


**Figure 2.1:** Reaction and decay tree selected for the simulation.

For the charge conjugate channel another 1.5 million events were generated. Table 2.1 shows the parameters used for the event generation.

For the production reaction $\bar{p}p \rightarrow \Xi(1820)^- \bar{\Xi}^+$ the PHSP (PHase SPace) model, generating an isotropic angular distribution, was used, because a more realistic treatment has not yet been implemented in EvtGen. This simplification does not affect the strategy used for this study.

**Table 2.1:** Parameter for event generation

| Parameter | Value |
|---|---|
| Beam momentum | 4.6 GeV/c |
| Production | PHSP |
| Tracking | Ideal |
| Particle ID | Ideal |

**Table 2.2:** Used software version

| Software | Version |
|---|---|
| FairSoft | mar15 |
| FairRoot | v-15.03a |
| PandaRoot | trunk revision 28555 |
| Geant | 3 |
| Genfit | 1 |

The chosen beam momentum $p_{\bar{p}} = 4.6\,\text{GeV/c}$ corresponds to a center-of-mass energy of 100 MeV above the production threshold of $\Xi(1820)^-$ and $\bar{\Xi}^+$. The production cross section is expected to be $\sigma(\bar{p}p \to \Xi(1820)^- \bar{\Xi}^+) \simeq 1\mu$b. This is in the same order as for ground state $\Xi^-$ production in $\bar{p}p \to \Xi^- \bar{\Xi}^+$ [1]. This expectation is based on ground state and excited state single strange hyperons production data in $\bar{p}p$ collisions [2].

The used software version for PandaRoot and the external software package is listed in table 2.2.

The $\Xi(1820)^-$ was defined in the evt.pdl file listing the properties of particles used in EvtGen. The properties of $\Xi(1820)^-$ are listed in table 2.3.

The distribution of the generated transverse momentum versus the longitudinal momentum for $\Lambda$ and $\bar{\Lambda}$ is presented in figure 2.2 and for $\bar{\Xi}^+$ and $\Xi(1820)^-$ in figure 2.3.

Figure 2.4 shows the Dalitz plot for the $\Lambda$, $K^-$ and $\bar{\Xi}^+$ final states for the channel $\bar{p}p \to \Xi(1820)^- \bar{\Xi}^+$.

The generated mass distribution for $\Xi(1820)^-$ is shown in figure 2.5. The mass of $\Xi(1820)^-$ is not fixed but has a mass distribution according to a Breit-Wigner distribution.

**Table 2.3:** Properties of $\Xi(1820)^-$. The values are taken from [3]

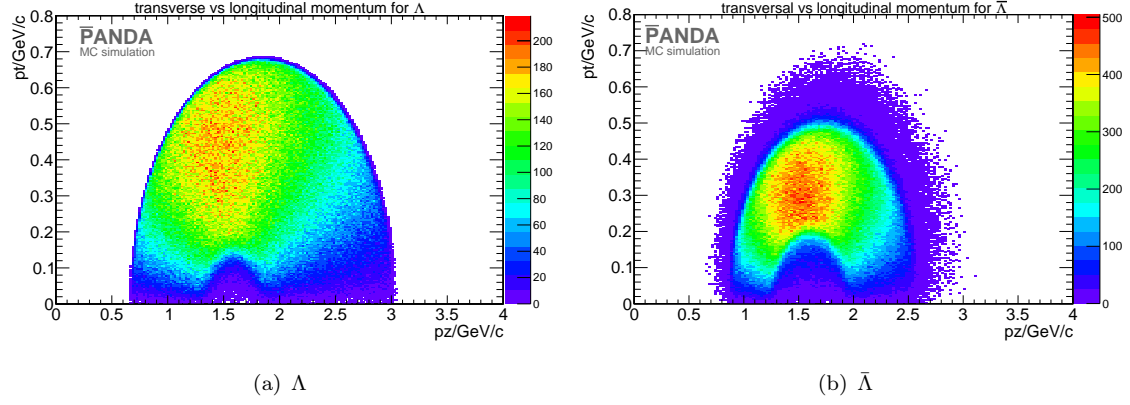| Particle | J | I | P | Charge | Mass | Width |
|---|---|---|---|---|---|---|
| $\Xi(1820)^-$ | $\frac{3}{2}$ | $\frac{1}{2}$ | $-1$ | $-1$ | $(1.823 \pm 5)$ GeV/c$^2$ | $(0.024 \pm 6)$ GeV/c$^2$ |

(a) Λ

(b) Λ̄

**Figure 2.2:** "PROPOSED FOR RELEASE" Figure a) shows the transverse momentum on the y axis versus the longitudinal momentum on the x axis for Λ. Figure b) shows the same distribution for Λ̄.
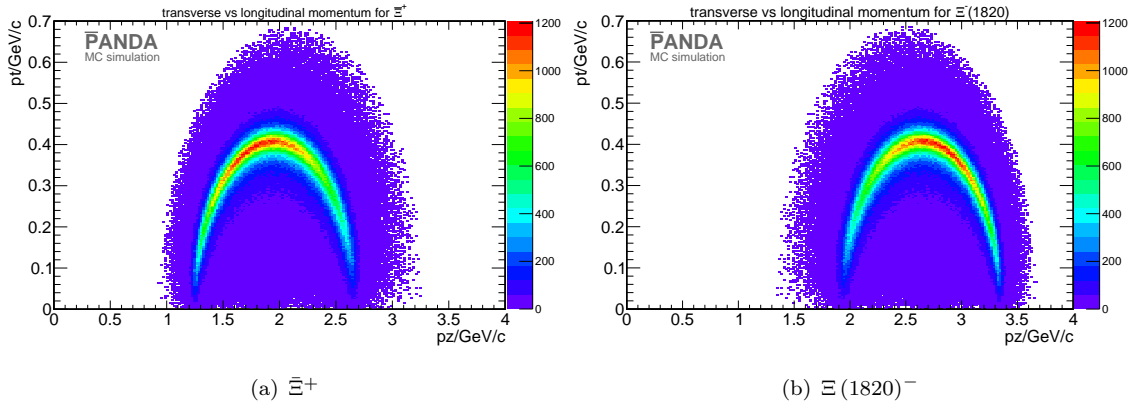


(a) Ξ̄⁺

(b) Ξ(1820)⁻

**Figure 2.3:** "PROPOSED FOR RELEASE" Figure a) shows transverse versus the longitudinal momentum distribution for Ξ̄⁺. Figure b): transverse versus longitudinal momentum distribution for Ξ(1820)⁻.
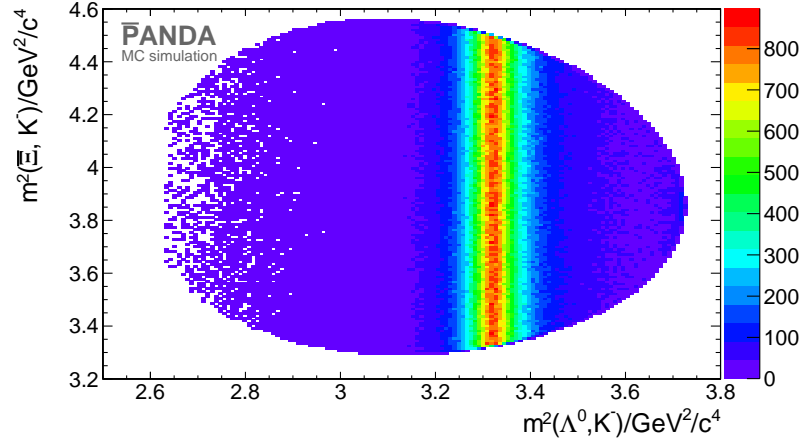
**Figure 2.4:** "PROPOSED FOR RELEASE" $\bar{\Xi}^+$ $\Lambda$ $K^-$ Dalitz plot for generated events. On the x axis is the squared mass of $\Lambda$ $K^-$ system and on the y axis there is the squared mass of $\bar{\Xi}^+$ $K^-$ system.
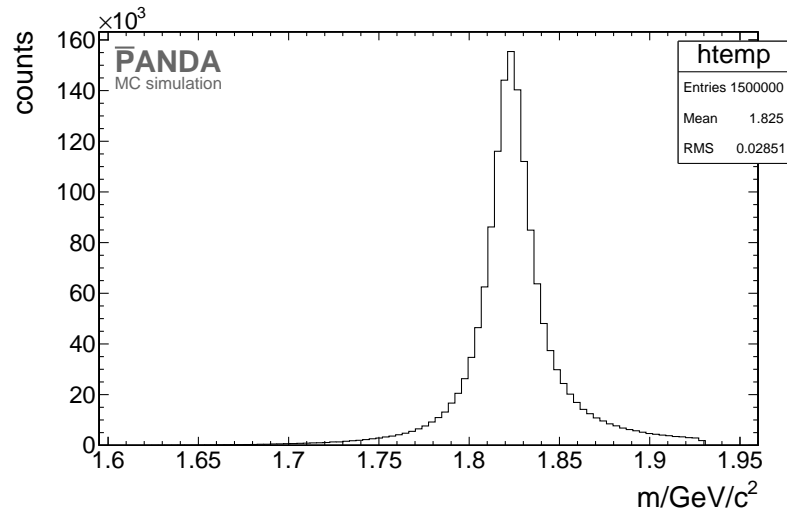


**Figure 2.5:** Generated mass distribution for $\Xi(1820)^-$ according to a Breit-Wigner distribution.

# 3 Analysis

To reconstruct all the particles involved in the reaction we start with the final state particles
and go backwards through the reaction chain.

## 3.1 Final state particles

The selected final state particle are protons, anti-protons, $\pi^-$, $\pi^+$, $K^-$ and $K^+$ mesons.
For the reconstruction of these particles an ideal tracking was used. Ideal tracking means
that the hit points caused by a particle track are grouped based on the generated particle
information. To achieve a more realistic reconstruction efficiency only particles with at
least 4 hits in any inner tracking detector (MVD, STT and GEM) are selected. The
selection criterion is chosen because three hits are needed to define a circle. A fourth hit
point is then a validation of the track hypothesis.
The particle identification (PID) is also ideal meaning that the true particle gets the
probability $P = 1$, the others $P = 0$. The selection criterion is set to 'best'.

The reconstruction efficiency and the momentum resolution for the final state particle is
shown in table 3.1 and figure 3.1. All reconstruction efficiencies are calculated with the
MC matched particles.
Table 3.2 shows the reconstruction efficiency and the momentum resolution for the charge
conjugate channel.

**Table 3.1:** "PROPOSED FOR RELEASE" Reconstruction efficiency and momentum resolution for $\bar{p}p \to \Xi(1820)^- \bar{\Xi}^+$. The errors are pure statistical errors.

| final state | N[%] | $\sigma_N^{\text{stat.}}$ [%] | $\frac{\sigma p}{p}$ [%] | $\sigma_{\frac{\sigma p}{p}}$ [%] |
|---|---|---|---|---|
| $\pi^-$ | 83.48 | 0.1 | 1.53 | $3 \cdot 10^{-3}$ |
| $\pi_1^+$ $(\bar{\Xi}^+)$ | 80.93 | 0.1 | 1.38 | $3 \cdot 10^{-3}$ |
| $\pi_2^+$ $(\bar{\Lambda})$ | 83.07 | 0.1 | 1.49 | $3 \cdot 10^{-3}$ |
| $K^-$ | 78.59 | 0.1 | 1.58 | $3 \cdot 10^{-3}$ |
| p | 84.39 | 0.1 | 1.61 | $4 \cdot 10^{-3}$ |
| $\bar{p}$ | 78.25 | 0.1 | 1.45 | $4 \cdot 10^{-3}$ |

**Table 3.2:** <span style="color:red">"PROPOSED FOR RELEASE"</span> Reconstruction efficiency and momentum resolution for $\bar{p}p \rightarrow \bar{\Xi}(1820)^{+}\,\Xi^{-}$. The errors are pure statistical errors.

| final state | N[%] | $\sigma_N^{\text{stat.}}\,[\%]$ | $\frac{\sigma p}{p}\,[\%]$ | $\sigma_{\frac{\sigma p}{p}}\,[\%]$ |
|---|---|---|---|---|
| $\pi^{+}$ | 82.96 | 0.1 | 1.54 | $2 \cdot 10^{-3}$ |
| $\pi_1^{-}\;(\Xi^{-})$ | 80.40 | 0.1 | 1.38 | $2 \cdot 10^{-3}$ |
| $\pi_2^{-}\;(\Lambda)$ | 82.69 | 0.1 | 1.49 | $3 \cdot 10^{-3}$ |
| $K^{+}$ | 83.27 | 0.1 | 1.58 | $3 \cdot 10^{-3}$ |
| p | 80.71 | 0.1 | 1.55 | $4 \cdot 10^{-3}$ |
| $\bar{p}$ | 80.93 | 0.1 | 1.60 | $4 \cdot 10^{-3}$ |


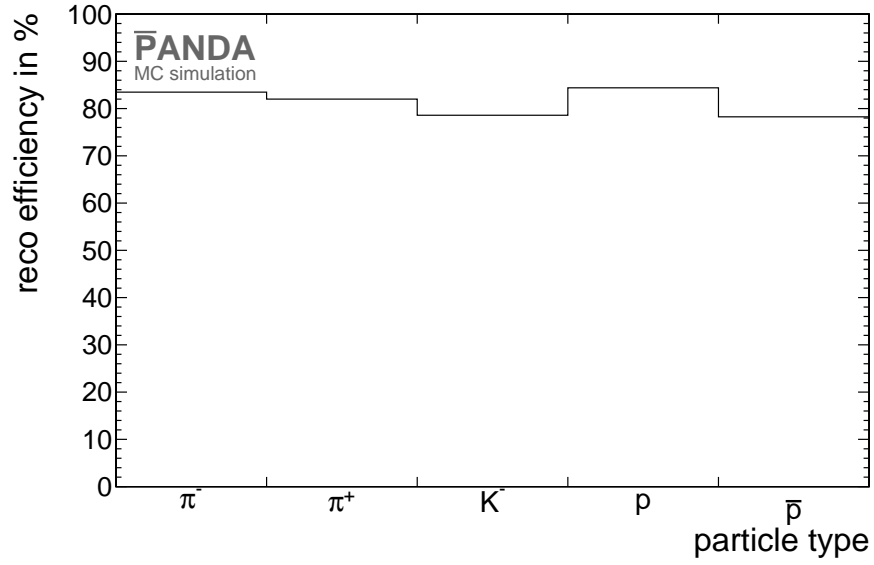
**Figure 3.1:** <span style="color:red">"PROPOSED FOR RELEASE"</span> Reconstruction efficiency for final state particles. The x axis shows the particle type. On the y axis the fraction of reconstructed particles is shown.
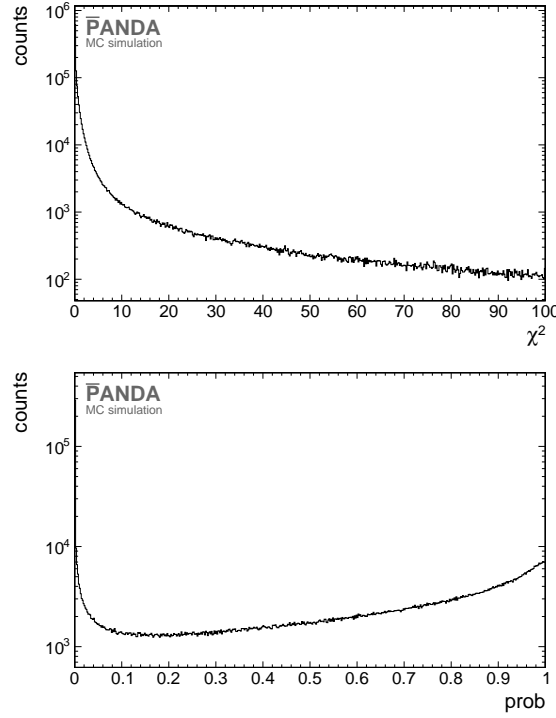
**Figure 3.2:** "PROPOSED FOR RELEASE" The upper plot shows the $\chi^2$ distribution and the lower plot shows the probability distribution for the $\Lambda$ vertex fit.

## 3.2 Reconstruction of $\Lambda$ and $\bar{\Lambda}$

### Selection

For the reconstruction of $\Lambda$ hyperons a proton and a $\pi^-$ meson are combined and for the reconstruction of $\bar{\Lambda}$ a $\bar{p}$ and a $\pi^+$ are combined. After combining the daughter particles a mass cut is performed. Only those candidates are chosen which have a mass within a window of $0.3\,\mathrm{GeV/c^2}$ symmetric to the nominal $\Lambda$ mass, i.e., a mass within $m = 1.116 \pm 0.15\,\mathrm{GeV/c^2}$.

A vertex constraint fit with the PndKinVtxFitter is performed on the selected candidate. This means that the tracks of the daughter particles are fitted to a common vertex point. The $\chi^2$ and probability distribution of the vertex fit for $\Lambda$ candidates is shown in figure 3.2.

In the probability distribution one can see an increasing number of events for probabilities approaching a value of one. To understand the origin of this behaviour the vertex fitter was tested with the "poormantrack" algorithm [4]. This algorithm creates simple particle tracks without using any detector information. The particle tracks were fitted to a common vertex point with the PndKinVtxFitter. These tests have shown that the behaviour of the
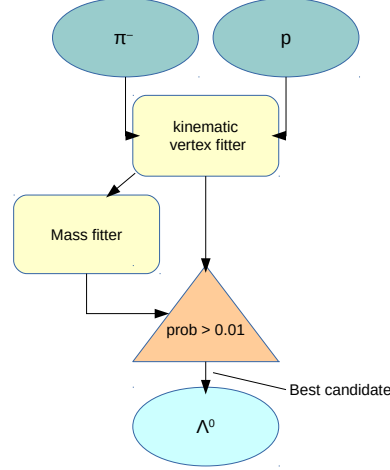
**Figure 3.3:** "PROPOSED FOR RELEASE" Scheme for Λ reconstruction

probability distribution is not caused by the PndKinVtxFitter code. The origin of this behaviour is still under investigation.

A mass constraint fit is performed on the fitted candidate. For this mass constraint fit the kinematic fitter PndKinFitter is used. After using both fitters the selection criterion is set. Only those particles which have a probability larger than 1% in both fitters are selected. A scheme which shows how the events are selected can be found in figure 3.3. If there is more than one candidate left after these cuts, the candidate with the lowest $\chi^2$ is chosen.

## Results

In this paragraph the Λ and Λ̄ sample obtained with the chosen selection criteria is presented. The mass distributions corresponding to the different cuts are shown in figure 3.4 and figure 3.5 for Λ and Λ̄, respectively.

The reconstructed mass can be determined by performing a double Gaussian fit on the mass distribution obtained after all cuts. The mass distribution and the double Gaussian fit are shown for Λ candidates in figure 3.6.

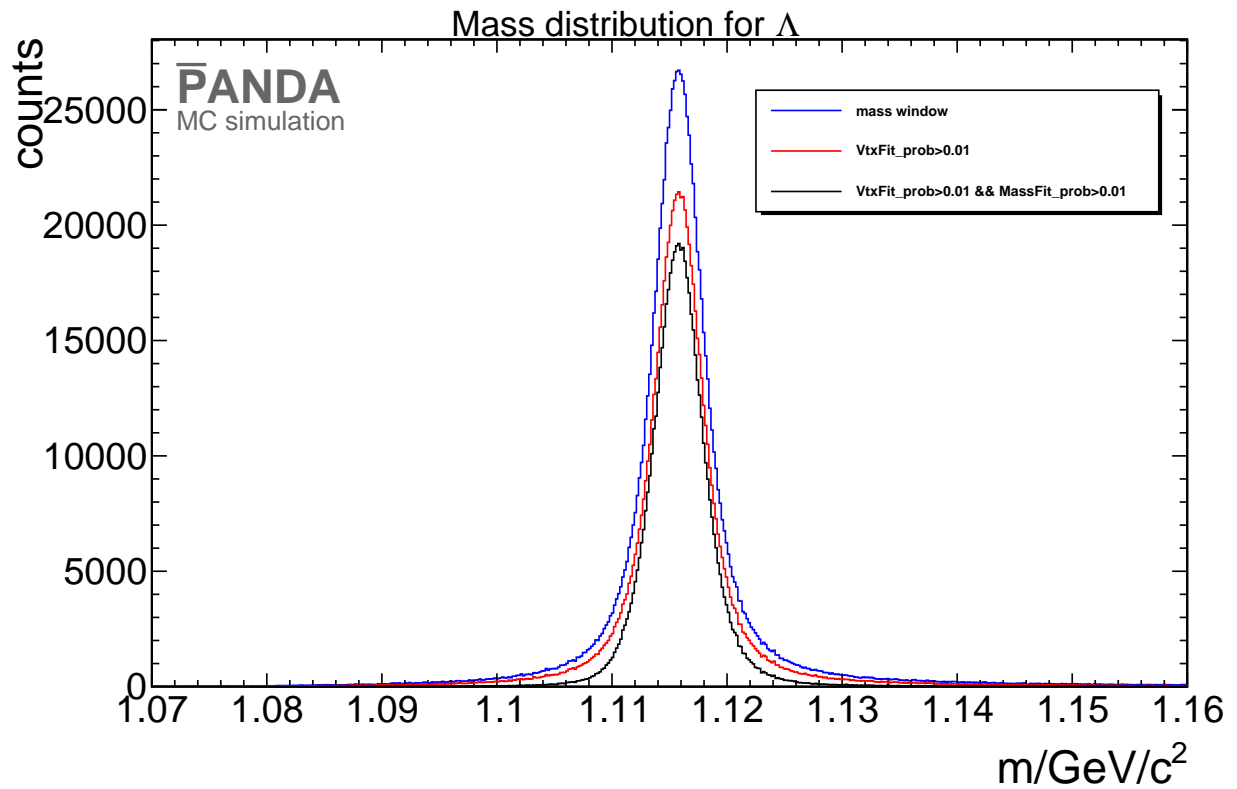The peak position of the Gaussian fit is taken as the value of the reconstructed mass. The

**Figure 3.4:** "PROPOSED FOR RELEASE" Mass distribution of Λ after the mass cut (blue), after the vertex fit cut (red) and after all cuts (black).
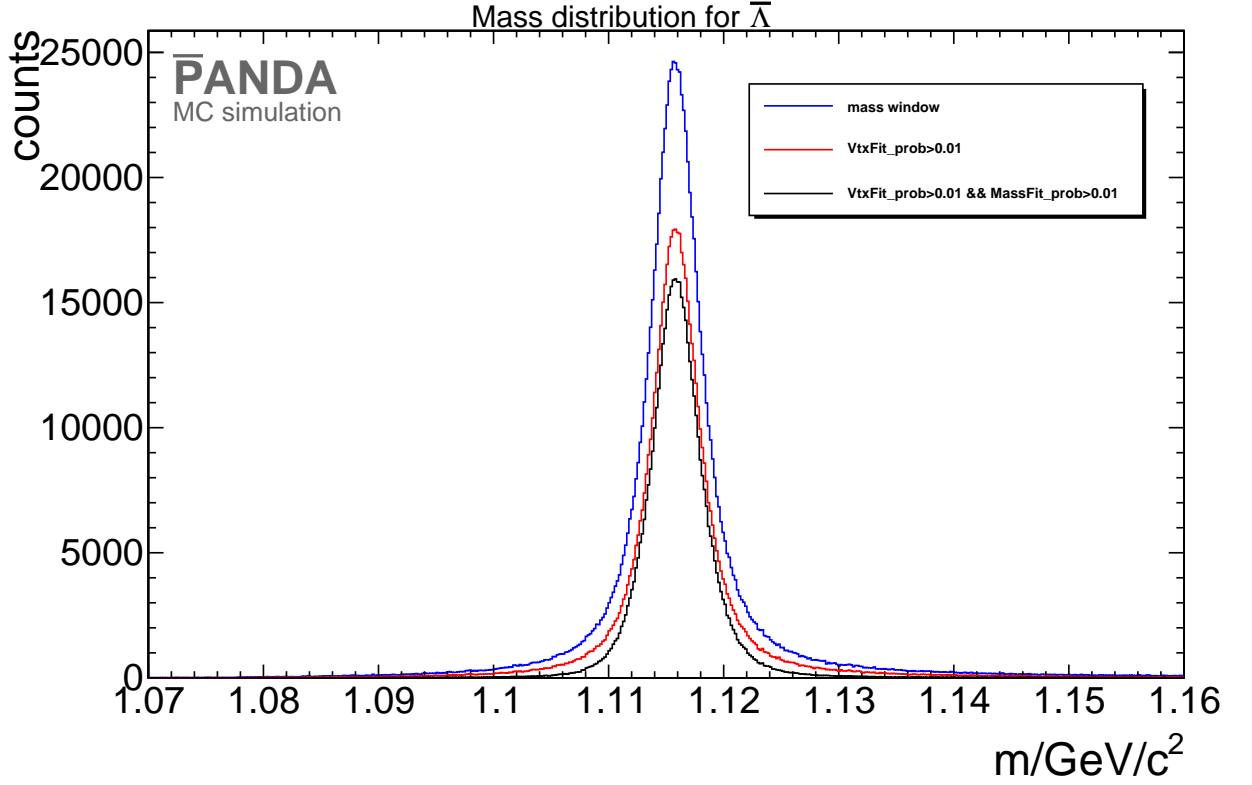
**Figure 3.5:** "PROPOSED FOR RELEASE" Mass distribution of $\bar{\Lambda}$ after the mass cut (blue), after the vertex fit cut (red) and after all cuts (black).
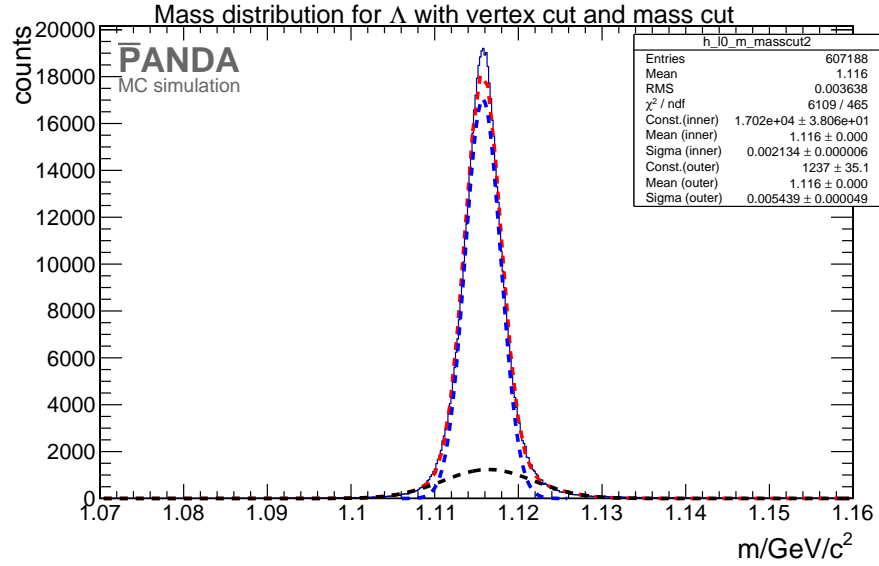


**Figure 3.6:** "PROPOSED FOR RELEASE" Mass distribution (blue histogram) for $\Lambda$ fitted with a double Gaussian fit (red dashed line). The inner Gaussian fit is shown as blue dashed line and the outer Gaussian fit as black dashed line.
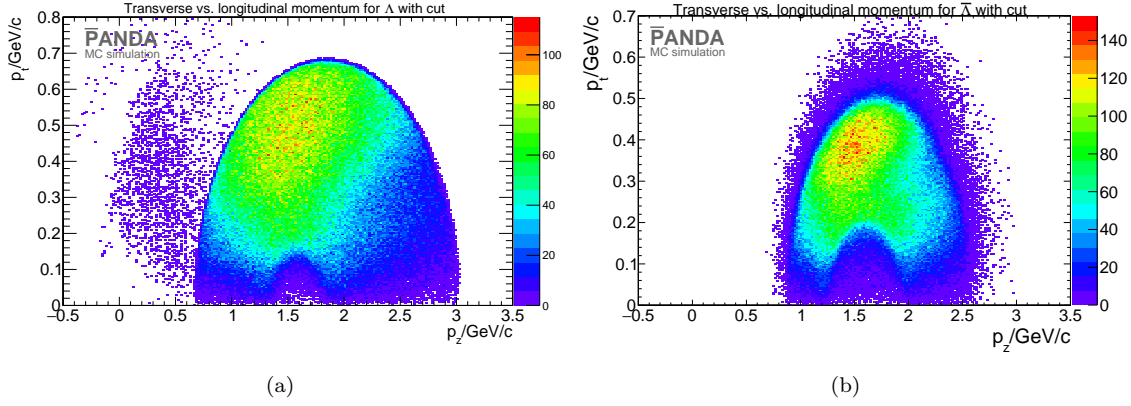
**Figure 3.7:** "PROPOSED FOR RELEASE" Figure a): transverse versus longitudinal momentum for $\Lambda$. Figure b):transverse versus longitudinal momentum for $\bar{\Lambda}$.

⁹⁶ reconstructed masses are $\mathrm{m}_\Lambda = (1.1158 \pm 0.0021)\,\mathrm{GeV/c^2}$ and $\mathrm{m}_{\bar{\Lambda}} = (1.1158 \pm 0.0021)\,\mathrm{GeV/c^2}$
⁹⁷ for $\Lambda$ and $\bar{\Lambda}$, respectively. Figure 3.7 shows the transverse momentum versus the longitu-
⁹⁸ dinal momentum.

⁹⁹ After all cuts the reconstruction efficiency is 40.48% for $\Lambda$ and 33.42% for $\bar{\Lambda}$. The difference
¹⁰⁰ in the reconstruction efficiencies for $\Lambda$ and $\bar{\Lambda}$ is caused by the different decay lengths of their
¹⁰¹ mother particles. $\Lambda$ is emitted by the $\Xi(1820)^-$ which has a very short decay length while
¹⁰² the decay length of $\bar{\Xi}^+$ is $c\tau = 4.91\,\mathrm{cm}$ [3]. The decay length of $\Lambda$ and $\bar{\Lambda}$ is $c\tau = 7.98\,\mathrm{cm}$,
¹⁰³ so that the final state particles of $\bar{\Lambda}$ are produced more downstream than the final state
¹⁰⁴ particles of $\Lambda$. This can be also seen in figure 3.8. The final state particles of $\bar{\Lambda}$ are produced
¹⁰⁵ at the edge of the MVD detector so that the reconstruction efficiency for these particles
¹⁰⁶ is reduced. An extension of the MVD with two more discs the so-called "Lambda-Discs"
¹⁰⁷ might improve the reconstruction efficiencies for $\Lambda$ and $\bar{\Lambda}$.

## 3.3 Reconstruction of $\Xi^-$ and $\bar{\Xi}^+$

### Selection

¹¹⁰ The reconstruction of $\Xi^-$ and $\bar{\Xi}^+$ follows a scheme similar to the reconstruction of $\Lambda$ and
¹¹¹ $\bar{\Lambda}$. For $\bar{\Xi}^+$ $\bar{\Lambda}$ and $\pi^+$ are recombined, for $\Xi^-$ in the charge conjugate channel $\Lambda$ and $\pi^-$.
¹¹² In case of the correct selection both the $\pi^-$ or $\pi^+$ candidate as daughter particle of $\Lambda$ or
¹¹³ $\bar{\Lambda}$, respectively, only one $\pi^-$ or $\pi^+$ candidate remains within the primary particles of the
¹¹⁴ reaction chain, which must be the daughter particle of $\Xi^-$ or $\bar{\Xi}^+$, respectively. The correct
¹¹⁵ selection of the $\Lambda$ and $\bar{\Lambda}$ daughter pions is assured by the choice of the best fitted $\Lambda$ and
¹¹⁶ $\bar{\Lambda}$ candidates, as described in section 3.2. The pions associated to the $\Lambda$ and $\bar{\Lambda}$ decay are
¹¹⁷ removed from the pion candidate lists used for the reconstruction of $\Xi^-$ and $\bar{\Xi}^+$. After
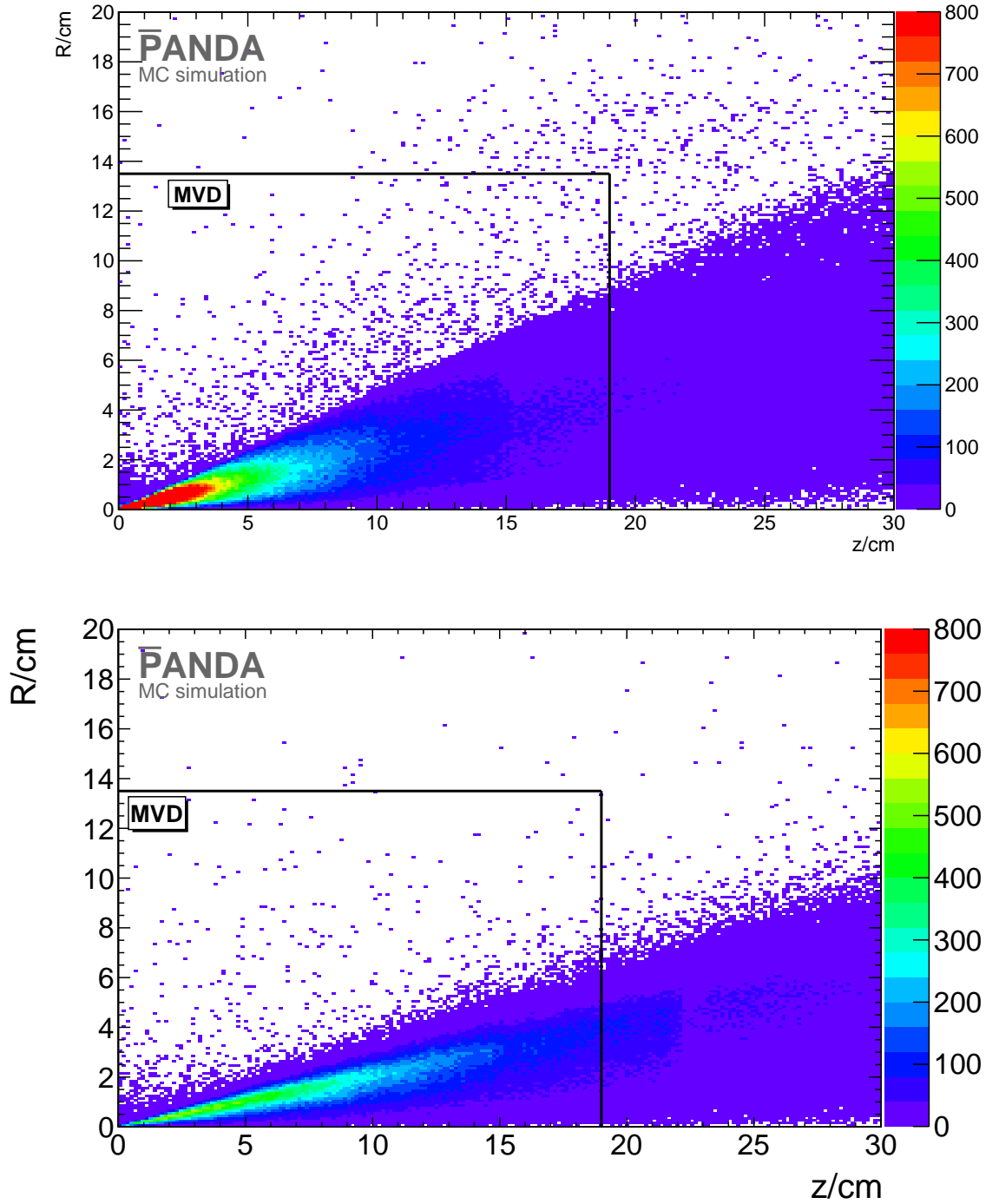
**Figure 3.8:** "PROPOSED FOR RELEASE" Decay vertex position of $\Lambda$ (upper plot) and $\bar{\Lambda}$ (lower plot). In both plots the x axis shows the z coordinate (along the beam axis) of the decay vertex while the y axis shows its radial coordinate (the origin of the coordinate system s defined by the primary vertex). The black horizontal and vertical lines mark the radial and longitudinal extension of the MVD.
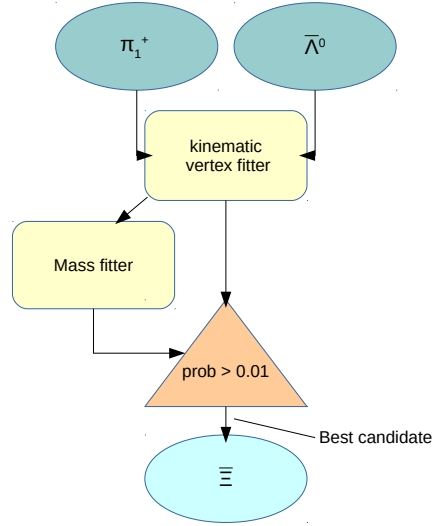
**Figure 3.9:** "PROPOSED FOR RELEASE" Scheme for $\bar{\Xi}^+$ reconstruction

combining the daughter particles a mass cut is performed corresponding to a window with
a width of $0.3\,\mathrm{GeV/c^2}$ symmetric around the $\Xi^-$ mass $m_\Xi = 1.32171$ GeV/c$^2$ [3].
The fitting scheme is the same as for $\Lambda$ and $\bar{\Lambda}$ and is shown in figure 3.9. After the mass
cut the daughter particles are fitted to a common vertex with the PndKinVtxFitter. The
resulting candidates are used to perform the mass constraint fit.
Only those particles are selected which have a probability of more than $1\,\%$ in both fitters.
Figure 3.10 shows exemplarily the cut on the vertex fit probability for $\bar{\Xi}^+$.
If there is more than one candidate left after all cuts, e.g. due to additional pions produced
in secondary interactions, the candidate with the lowest $\chi^2$ is chosen.

## Results

The vertex resolution after all cuts is shown in table 3.3.
It is determined by calculating the full width at half maximum (FWHM) of the distribution.
The advantage of using this method for calculating the vertex resolution is that the FWHM
is independent of the shape of the distribution. Figures 3.11 and 3.12 show the vertex
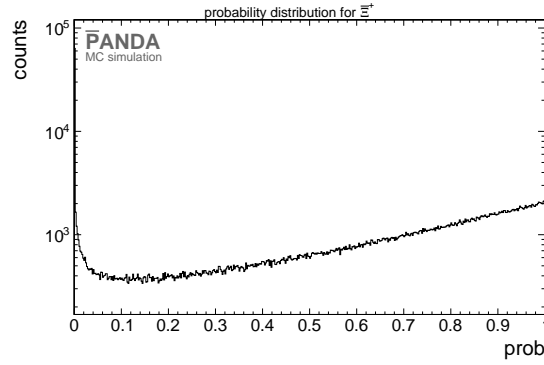resolution distribution.

**Figure 3.10:** "PROPOSED FOR RELEASE" probability distribution for $\bar{\Xi}^+$ reconstruction.

**Table 3.3:** "PROPOSED FOR RELEASE" Vertex resolution for $\bar{\Xi}^+$ and $\Xi^-$ (charge conjugate. channel)

| position | $\bar{\Xi}^+$ | $\Xi^-$ (from charge conjugate.) |
|---|---|---|
| x/cm | 0.052 | 0.056 |
| y/cm | 0.052 | 0.052 |
| z/cm | 0.19 | 0.2 |



(a) Vertex resolution for x coordinate
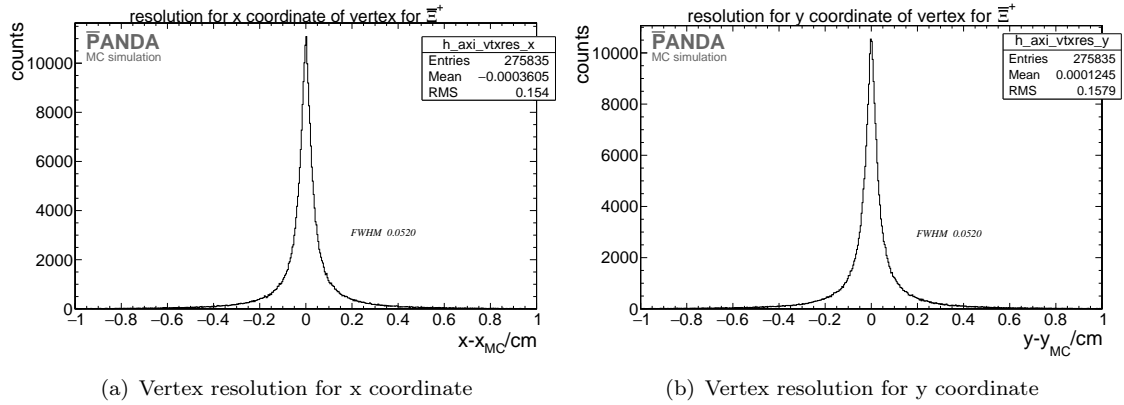
(b) Vertex resolution for y coordinate

**Figure 3.11:** "PROPOSED FOR RELEASE" The left plot shows the vertex resolution in the x coordinate for $\bar{\Xi}^+$. The right plot shows the vertex resolution of in the y coordinate for $\bar{\Xi}^+$.
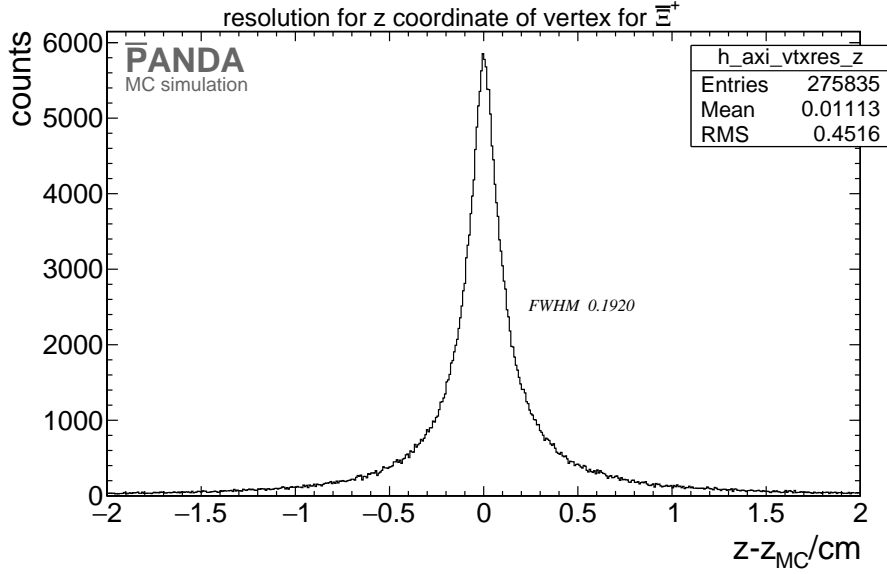
**Figure 3.12:** "PROPOSED FOR RELEASE" Vertex resolution of in the z coordinate for
$\bar{\Xi}^+$ candidates.

The mass distribution obtained with the different cuts is shown in figure 3.13 and figure
3.14 for $\bar{\Xi}^+$ and $\Xi^-$, respectively. The number of events is strongly reduced by the cut on
the vertex fit probability. The width of the mass distribution is reduced.

After using all cuts on the mass distribution the reconstructed mass of $\Xi^-$ and $\bar{\Xi}^+$ can be
determined by a double Gaussian fit. This is exemplarily shown for the $\Xi^-$ in figure 3.15.
The result of the mass fit is for $\bar{\Xi}^+$ m $= (1.322 \pm 0.004)$ GeV/c$^2$ and for $\Xi^-$
m $= (1.322 \pm 0.004)$ GeV/c$^2$. The two dimensional momentum distribution for $\bar{\Xi}^+$ and $\Xi^-$
is shown in figure 3.16

The reconstruction efficiency for $\bar{\Xi}^+$ is 18.4% and for $\Xi^-$ 18.6%.

## 3.4 Reconstruction of $\Xi(1820)^-$ and $\bar{\Xi}(1820)^+$

**Selection**

For the reconstruction of $\Xi(1820)^-$ one combines the $\Lambda$ candidate with the K$^-$ meson
candidate and for $\bar{\Xi}(1820)^+$ $\bar{\Lambda}$ and K$^+$, using the fit candidates $\Lambda$ and $\bar{\Lambda}$. After the
combination of the particles a mass cut with a width of $0.3$ GeV/c$^2$ symmetric to the
nominal $\Xi(1820)^-$ mass is performed. The daughter particles are then fitted to a common
vertex point with the PndKinVtxFitter. Only those candidates for $\Xi(1820)^-$ ($\bar{\Xi}(1820)^+$)
are selected which have a fit probability of more then 1%. The selection scheme is shown
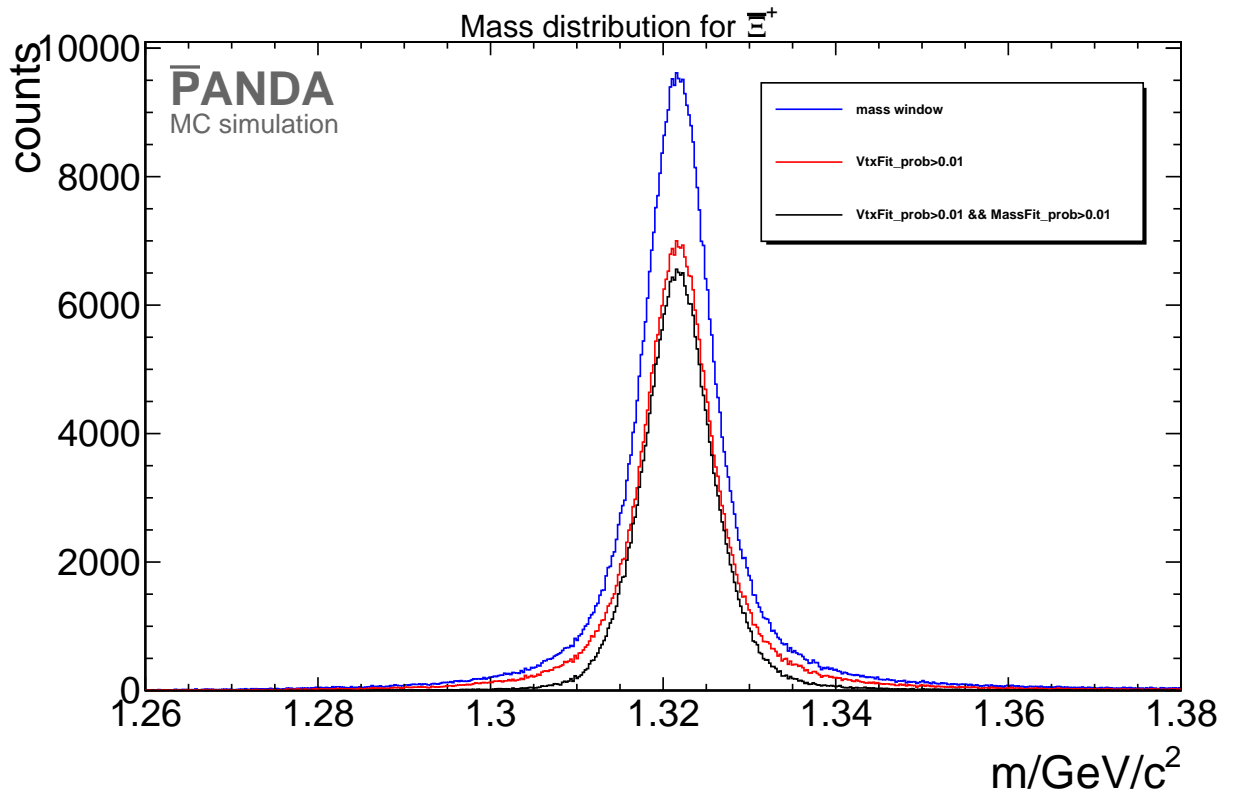in figure 3.17.

**Figure 3.13:** "PROPOSED FOR RELEASE" Mass distribution of the $\bar{\Xi}^+$ after after the mass cut (blue), after the vertex fit cut (red) and after all cuts (black).

**Figure 3.14:** "PROPOSED FOR RELEASE" Mass distribution of the $\Xi^-$ after after the mass cut (blue), after the vertex fit cut (red) and after all cuts (black).

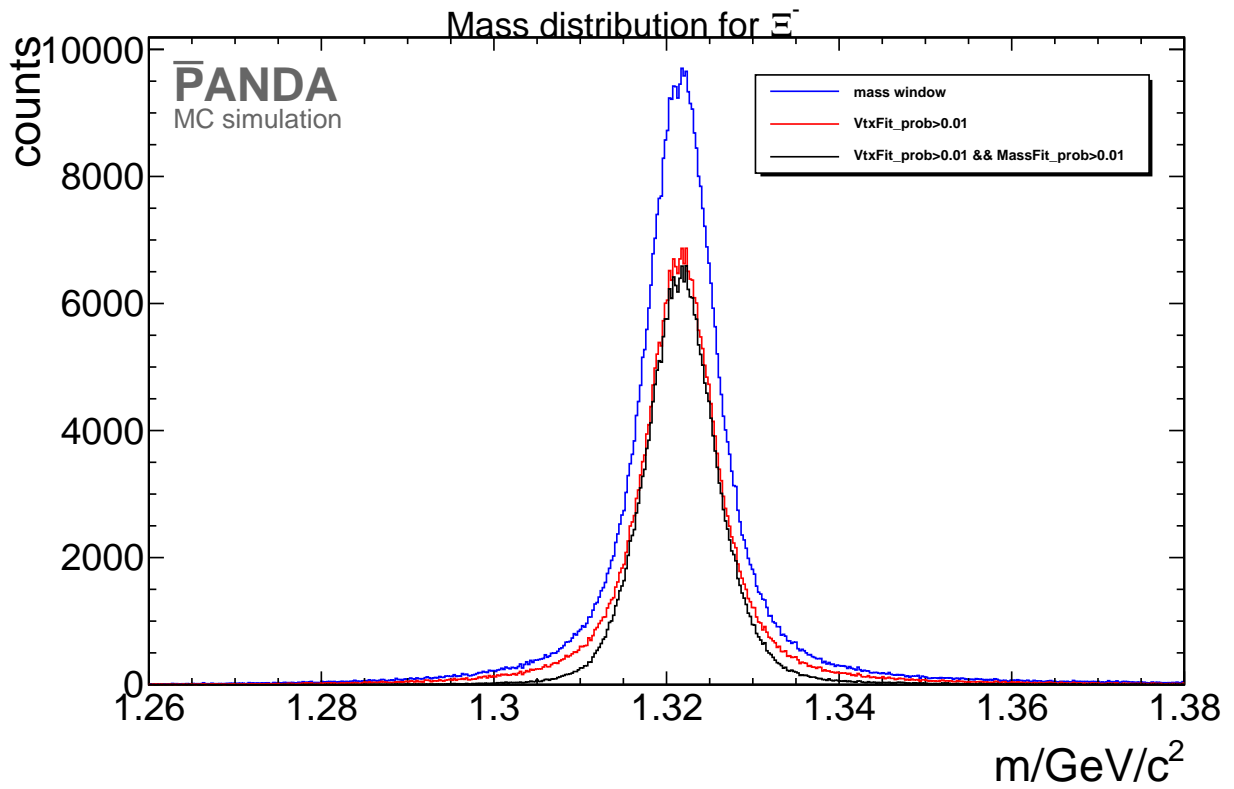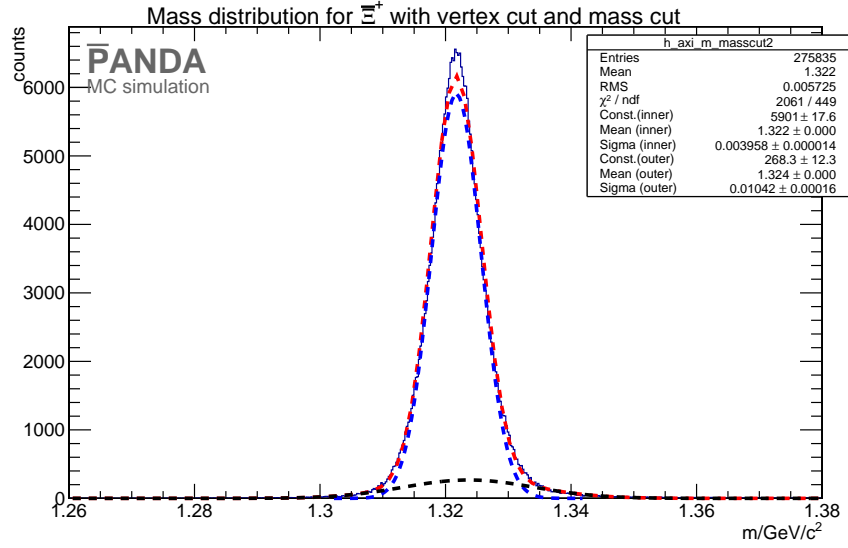**Figure 3.15:** "PROPOSED FOR RELEASE" The plot shows the mass distribution (blue histogram) after all cuts. A double Gaussian fit (red dashed line) is performed to determine the mean reconstructed mass for the $\bar{\Xi}^+$. The inner Gaussian fit is shown as blue dashed line and the outer Gaussian fit as black dashed line.



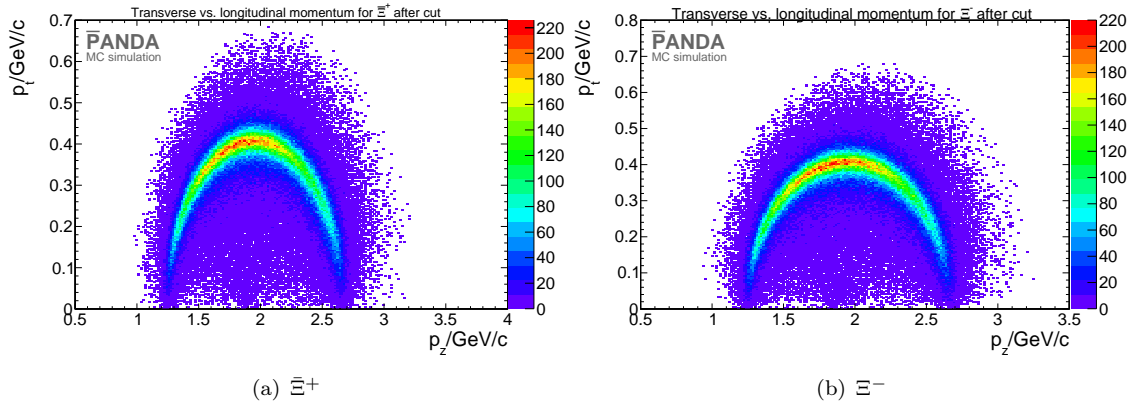(a) $\bar{\Xi}^+$

(b) $\Xi^-$

**Figure 3.16:** "PROPOSED FOR RELEASE" The plots shows the transverse versus the longitudinal momentum for $\bar{\Xi}^+$ and $\Xi^-$ after vertex fit and mass fit.
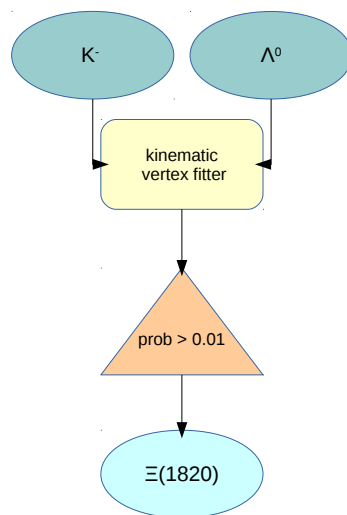
**Figure 3.17:** "PROPOSED FOR RELEASE" Scheme for $\Xi(1820)^-$ reconstruction
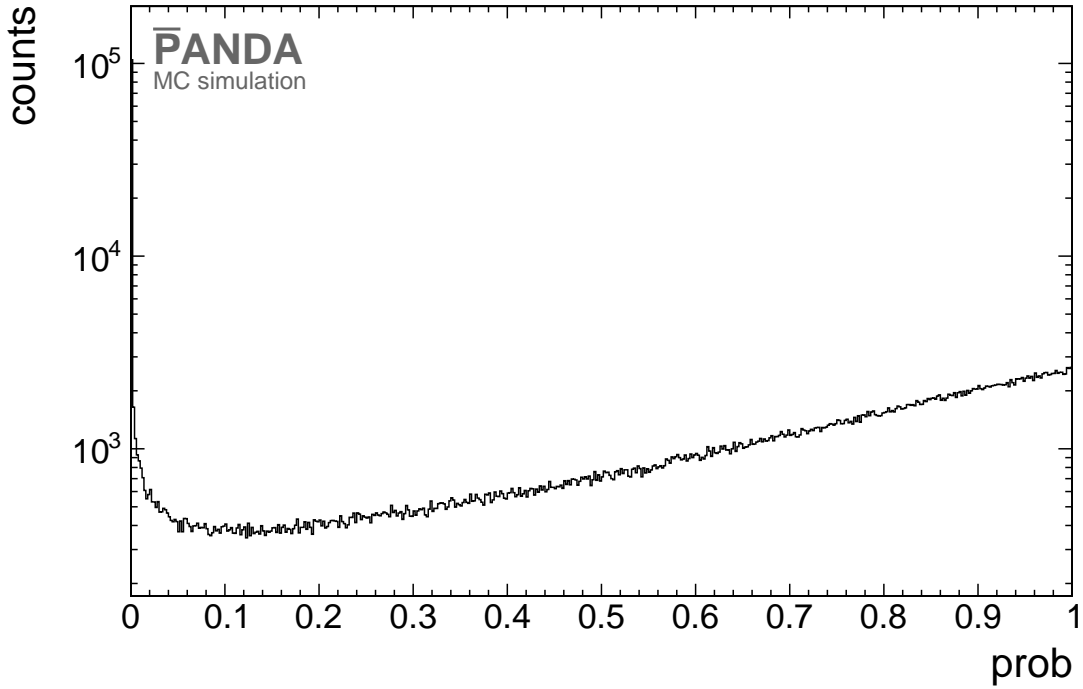
**Figure 3.18:** "PROPOSED FOR RELEASE" probability distribution of the kinematic vertex fit for $\Xi\,(1820)^-$ candidates.

**Table 3.4:** "PROPOSED FOR RELEASE" Vertex resolution for $\Xi\,(1820)^-$ and $\bar{\bar{\Xi}}\,(1820)^+$.

| position | $\Xi\,(1820)^-$ | $\bar{\bar{\Xi}}\,(1820)^+$ (from charge conjugate.) |
|:---:|:---:|:---:|
| x/cm | 0.028 | 0.028 |
| y/cm | 0.028 | 0.028 |
| z/cm | 0.1 | 0.1 |

151  The probability distribution for the vertex fit is shown in figure 3.18. Again the distribution
152  is not flat but increases for values close to one.

153  If there is more than one particle the fit candidate with the smallest $\chi^2$ is chosen.

## Results

155  The vertex resolution for $\Xi\,(1820)^-$ and $\bar{\bar{\Xi}}\,(1820)^+$ is summarized in table 3.4.

156  Here again the vertex resolution is measured using the FWHM of the distribution. This is
157  shown for $\Xi\,(1820)^-$ in figure 3.19 and 3.20.

158  After performing both fits and cut on the probability values, the mass for $\Xi\,(1820)^-$ and
159  $\bar{\bar{\Xi}}\,(1820)^+$ can be determined by fitting with a double Gaussian function. Figure 3.21 shows
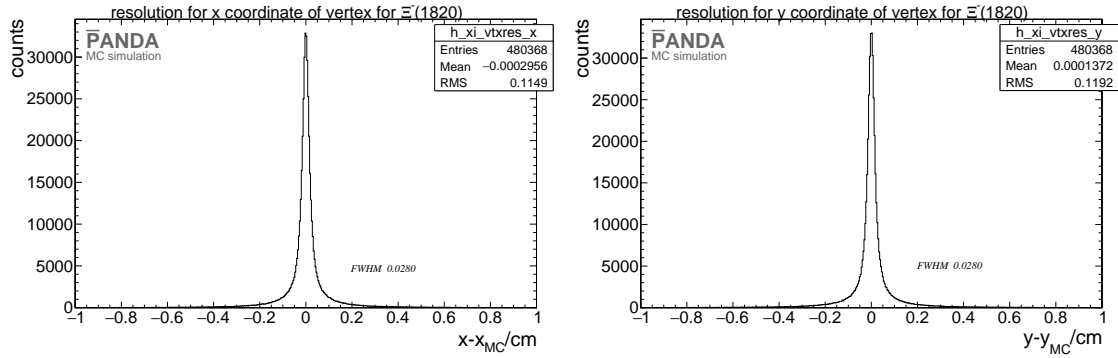
(a) Vertex resolution of the x coordinate for $\Xi(1820)^-$. (b) Vertex resolution of the y coordinate for $\Xi(1820)^-$.

**Figure 3.19:** "PROPOSED FOR RELEASE" Figure a) shows the vertex resolution for the x coordinate and figure b) for the y coordinate of $\Xi(1820)^-$
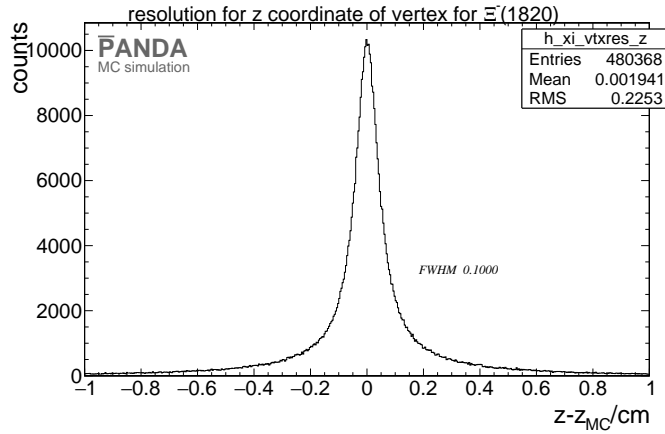


**Figure 3.20:** "PROPOSED FOR RELEASE" Vertex resolution in the z coordinate for $\Xi(1820)^-$.
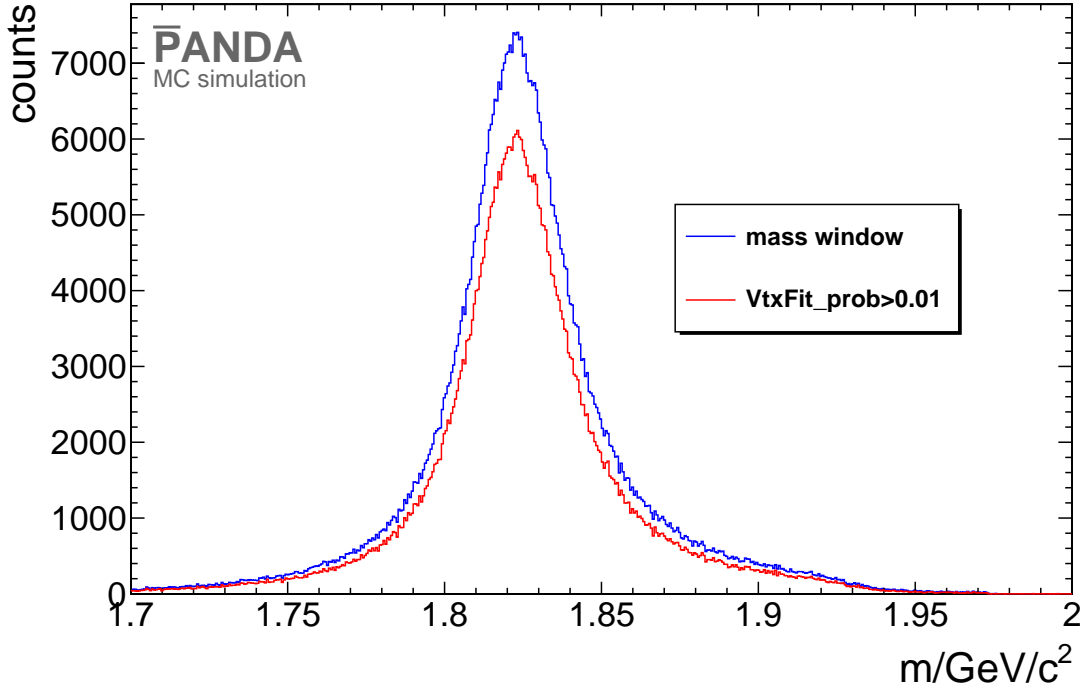
**Figure 3.21:** "PROPOSED FOR RELEASE" Mass distribution for $\Xi(1820)^-$ after the mass cut in blue and after the vertex fit probability cut in red.

160   the mass distribution for both particles after each cut.

161   As an example the mass fit is shown for the $\Xi(1820)^-$ in figure 3.22.

162   The mass value for the $\Xi(1820)^-$ is fitted to $m_{\Xi^*} = (1.823 \pm 0.014))$ GeV/c$^2$ and for

163   $\bar{\Xi}(1820)^+$ to $m_{\bar{\Xi}^*} = (1.823 \pm 0.014)$ GeV/c$^2$. These values are close to the input value.

164   Figure 3.23 shows the two-dimensional momentum distribution of $p_t$ versus $p_z$.

165   The reconstructed distributions are in good agreement with the distribution obtained for

166   the generated events which are shown in figure 2.3 (b).
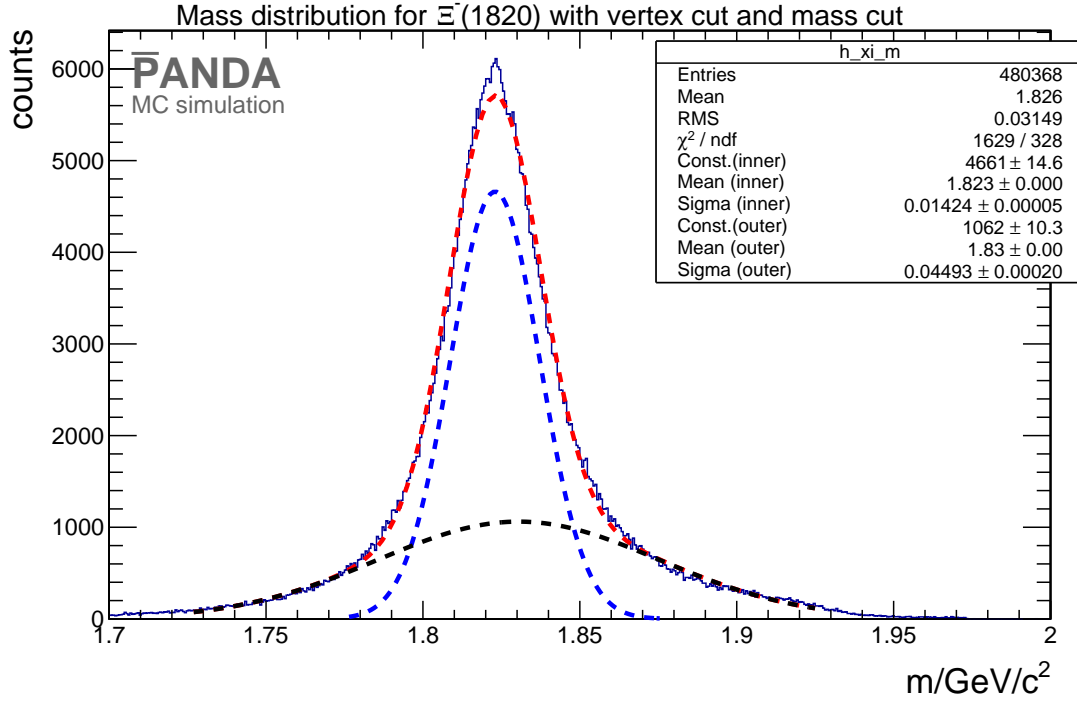
**Figure 3.22:** "PROPOSED FOR RELEASE" Mass distribution (blue histogram) after
all cuts for $\Xi(1820)^-$. The performed double Gaussian fit is shown as the
red dashed line. The inner Gaussian fit is shown as blue dashed line and
the outer Gaussian fit as black dashed line.



(a) $\Xi(1820)^-$

(b) $\bar{\Xi}(1820)^+$

**Figure 3.23:** "PROPOSED FOR RELEASE" Both plots show the longitudinal versus
the transverse momentum of the excited cascade baryon and its antiparticle,
respectively.

**Figure 3.24:** "PROPOSED FOR RELEASE" 4-constraint fit probability. The red line denotes the cut value of 1%.

## 3.5 Reconstruction of the whole reaction chain

### Selection

To reconstruct the whole reaction chain $\Xi(1820)^-$ and $\bar{\Xi}^+$ are combined. This is also done with $\bar{\Xi}(1820)^+$ and $\Xi^-$ for the charge conjugated channel. For this reconstruction the event sele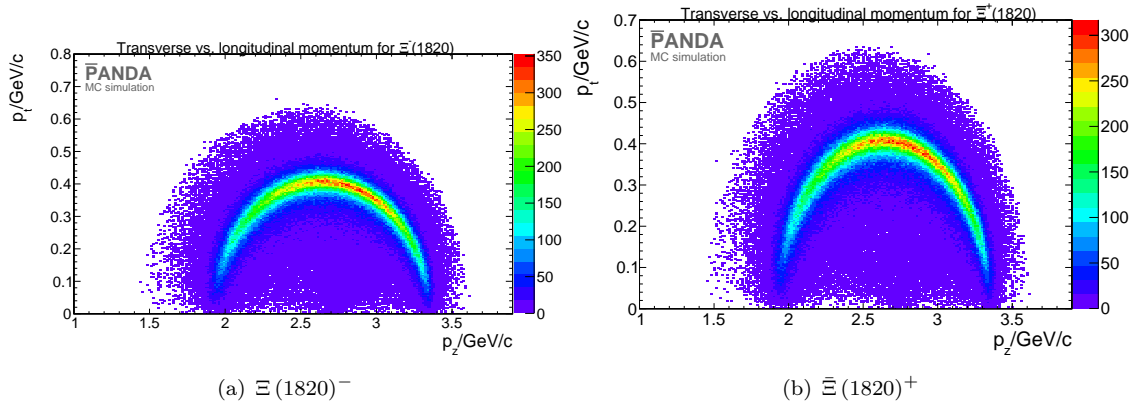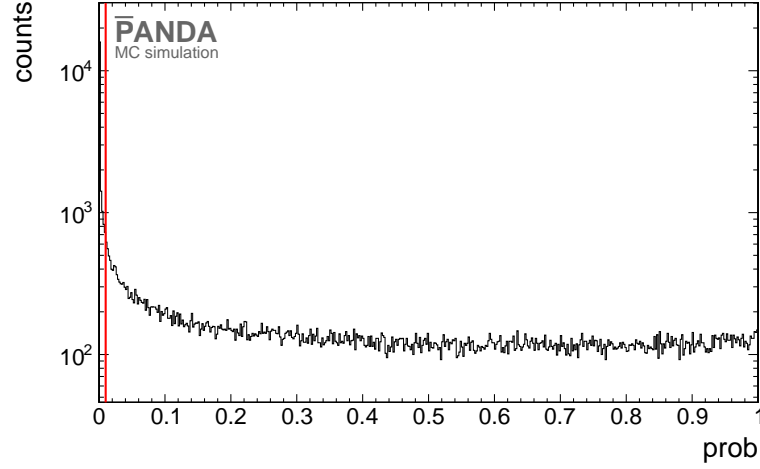ction is done with an exclusive method. The resulting four-momentum vector of both daughter particles – here $\Xi(1820)^-$ and $\bar{\Xi}^+$ and their charge conjugate particles – is fitted with the constraint to match to the initial four momentum vector

$$\left(\mathrm{p}_x,\ \mathrm{p}_y,\ \mathrm{p}_z,\ \mathrm{E}\right) = (0,\ 0,\ 4.6,\ 5.63)\ \mathrm{GeV}$$

of the $\bar{\mathrm{p}}\mathrm{p}$ entrance channel. This fit is performed with the PndKinFitter. After the four-momentum fit only those candidates are selected which have a probability of more than 1%. The probability is shown in figure 3.24. The red line denotes the cut value.
The selection scheme is shown in figure 3.25

### Results

The obtained reconstruction efficiency for all intermediate state particles is shown in table 3.5 and table 3.6.
The total numbers of intermediate state particles in $\bar{\mathrm{p}}\mathrm{p} \to \Xi(1820)^- \bar{\Xi}^+$ and $\bar{\mathrm{p}}\mathrm{p} \to \bar{\Xi}(1820)^+ \Xi^-$ are shown in table 3.7 and 3.8.
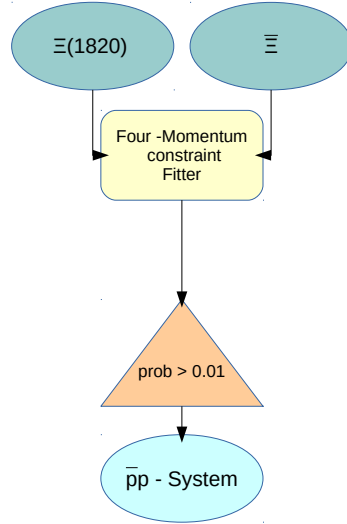
**Figure 3.25:** "PROPOSED FOR RELEASE" Scheme for the reconstruction of the whole reaction chain.

**Table 3.5:** "PROPOSED FOR RELEASE" reconstruction efficiency for intermediate state particles for $\bar{p}p \to \Xi(1820)^- \bar{\Xi}^+$

| particle | reco. efficiency [%] | dp/p [%] |
|---|---|---|
| $\Lambda$ | 40.5 | 1.40 |
| $\bar{\Lambda}$ | 33.4 | 1.49 |
| $\bar{\Xi}^+$ | 18.4 | 1.29 |
| $\Xi(1820)^-$ | 32.0 | 2.68 |
| $\Xi(1820)^- \bar{\Xi}^+$ system | 4.7 | 1.03 |

**Table 3.6:** "PROPOSED FOR RELEASE" Reconstruction efficiency for intermediate state particles for $\bar{p}p \to \bar{\Xi}(1820)^+ \Xi^-$

| particle | reco. efficiency [%] | dp/p [%] |
|---|---|---|
| $\Lambda$ | 32.8 | 1.44 |
| $\bar{\Lambda}$ | 40.8 | 1.46 |
| $\Xi^-$ | 18.6 | 2.30 |
| $\bar{\Xi}(1820)^+$ | 33.2 | 1.31 |
| $\bar{\Xi}(1820)^+ \Xi^-$ system | 4.9 | 1.03 |

**Table 3.7:** "PROPOSED FOR RELEASE" number of intermediate state particles for $\bar{\mathrm{p}}\mathrm{p} \rightarrow \Xi\,(1820)^- \bar{\Xi}^+$ including the branching ratios $\mathrm{BR}(\Lambda \rightarrow \pi^- \mathrm{p}) = 0.639$, $\mathrm{BR}(\Xi^- \rightarrow \Lambda\,\pi^-) = 0.999$ and $\mathrm{BR}(\Xi\,(1820)^- \rightarrow \Lambda\,\mathrm{K}^-) = 0.3$.

| particle | $N_{\mathrm{sig}}$ |
|---|---|
| $\Lambda$ | 387,993 |
| $\bar{\Lambda}$ | 320,316 |
| $\bar{\Xi}^+$ | 176,840 |
| $\Xi\,(1820)^-$ | 306,955 |
| $\Xi\,(1820)^- \bar{\Xi}^+$ | 8614 |

**Table 3.8:** "PROPOSED FOR RELEASE" number of intermediate state particles for $\bar{\mathrm{p}}\mathrm{p} \rightarrow \Xi\,(1820)^- \bar{\Xi}^+$ including the branching ratios $\mathrm{BR}(\bar{\Lambda} \rightarrow \pi^+ \bar{\mathrm{p}}) = 0.639$, $\mathrm{BR}(\bar{\Xi}^+ \rightarrow \bar{\Lambda}\,\pi^+) = 0.999$ and $\mathrm{BR}(\bar{\Xi}\,(1820)^+ \rightarrow \bar{\Lambda}\,\mathrm{K}^+) = 0.3$.

| particle | $N_{\mathrm{sig}}$ |
|---|---|
| $\Lambda$ | 314,807 |
| $\bar{\Lambda}$ | 390,660 |
| $\Xi^-$ | 173,510 |
| $\bar{\Xi}\,(1820)^+$ | 318,450 |
| $\bar{\Xi}\,(1820)^+ \Xi^-$ | 8943 |

These numbers are including the branching ratios for the single decays from [3]: $\mathrm{BR}(\Lambda \rightarrow \pi^- \mathrm{p}) = 0.639$ and $\mathrm{BR}(\Xi^- \rightarrow \Lambda\,\pi^-) = 0.999$. For $\Xi\,(1820)^-$ the branching ratio is assumed to be $\mathrm{BR}(\Xi\,(1820)^- \rightarrow \Lambda\,\mathrm{K}^-) = 0.3$.

Figure 3.26 shows the Dalitz plot for the $\bar{\Xi}^+$, $\Lambda$ and $\mathrm{K}^-$ final states after the reconstruction before the 4-C kinematic fit. Figure 3.26 should be compared with the Dalitz plot of the generated particles shown in figure 2.4 in order to assess the quality of the reconstruction procedure.

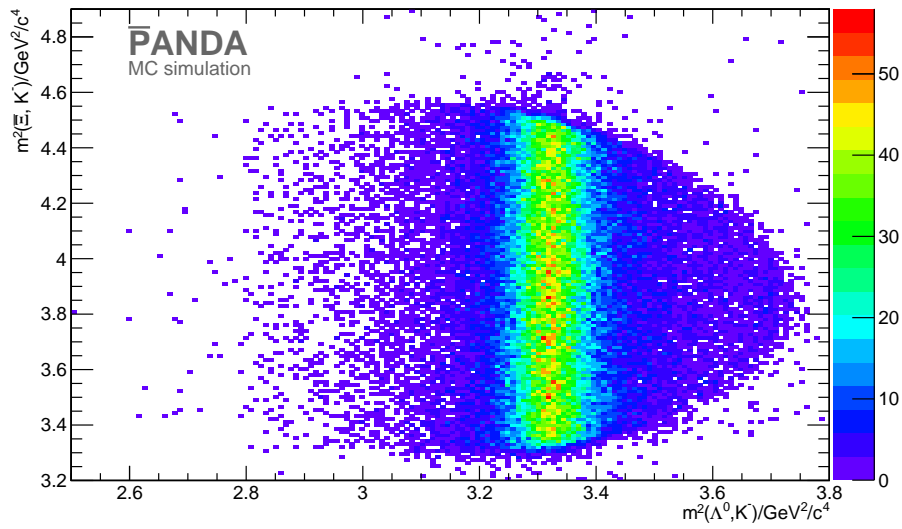**Figure 3.26:** "PROPOSED FOR RELEASE" Dalitz plot for reconstructed $\bar{\Xi}^+ \Lambda K^-$ final state.

# 4 Background

For background studies 15 million events have been simulated with the Dual Parton Model based generator DPM. To compare the number of selected events of background and signal, a scaling factor is needed. This scaling factor can be calculated with the number of generated events and the cross section of signal and background.

$$B = \frac{N_{\text{sig}}^{\text{gen}}/\sigma_{\text{sig}}}{N_{\text{bg}}^{\text{gen}}/\sigma_{\text{bg}}}, \tag{4.0.1}$$

where $N_{\text{sig}}^{\text{gen}}$ is the number of generated signal events and $N_{\text{bg}}^{\text{gen}}$ the number of generated background events. The signal and background cross sections are given by $\sigma_{\text{sig}} = 1\,\mu\text{b}$ [1] and $\sigma_{\text{bg}} = 60\,\text{mb}$ [3], respectively. The scaling factor is $B = 6000$ for the channel $\bar{\text{p}}\text{p} \to \Xi(1820)^- \bar{\Xi}^+$. The scaling factor for the c.c. channel is the same. This means that the number of reconstructed events in the background sample surviving all cuts applied to the reconstruction of the signal events has to be multiplied by a factor 6000 in order to deduce the achieved signal-to-background ratio.

All background events are subject to the same reconstruction procedure including all cuts for the signal events. The number of reconstructed background events is shown in table 4.1.

The comparison between signal and background events is shown in table 4.2. The significance is given by

$$S = \frac{N_{\text{sig}}}{\sqrt{N_{\text{sig}} + N_{\text{bg}} \cdot B}}. \tag{4.0.2}$$

**Table 4.1:** Number of reconstructed particles in the background sample for $\bar{\text{p}}\text{p} \to \Xi(1820)^- \bar{\Xi}^+$

| Particle | $N_{\text{bg}}$ |
|---|---|
| $\Lambda$ | 264,142 |
| $\bar{\Lambda}$ | 124,068 |
| $\bar{\Xi}^+$ | 3,062 |
| $\Xi(1820)^-$ | 298 |
| $\Xi(1820)^- \bar{\Xi}^+$ | 0 |

**Table 4.2:** "PROPOSED FOR RELEASE" The number of background events scaled with factor $B$ compared to the number of signal events for $\bar{p}p \rightarrow \Xi(1820)^- \bar{\Xi}^+$. The significance is calculated with equation 4.0.2.

| Particle | $N_{\text{sig}}$ | $N_{\text{bg}} \cdot B$ | $S$ |
|---|---|---|---|
| $\Lambda$ | 387,993 | $1.585 \cdot 10^9$ | 9.7 |
| $\bar{\Lambda}$ | 320,316 | $744.408 \cdot 10^6$ | 11.7 |
| $\bar{\Xi}^+$ | 176,840 | $18.372 \cdot 10^6$ | 41 |
| $\Xi(1820)^-$ | 306,955 | $1.788 \cdot 10^6$ | 212.1 |
| $\Xi(1820)^- \bar{\Xi}^+$ | 8,614 | $< 6,000$ | $> 71.3$ |

Because none of the background events survives the cuts applied to reconstruct the signal, it is only possible to estimate a lower limit for the significance. For one background event scaled by the factor $B$ the significance is at least 71.3. The signal-to-background ratio is for this estimation

$$\frac{N_{\text{sig}}}{N_{\text{bg}}} = \frac{8,614}{6,000} = 1.44 : 1$$

The values for the significance are unrealistically high since they are obtained from ideal tracking and ideal particle identification. For the final numbers one have to use a more realistic software. Additionally for a more precise statement more background studies have to be done.

# 5 Summary and Conclusion

The complete reaction chain can be reconstructed with an efficiency of about 5% for $\bar{\text{p}}\text{p}$ $\rightarrow \Xi\left(1820\right)^{-}$ and $\bar{\Xi}^{+}$ and its charge conjugate channel.

Each final states particle has a reconstruction efficiency of nearly 80%. The reconstruction of $\Lambda$ and $\bar{\Lambda}$ shows a difference in the efficiencies. This is caused by the different mother particles of the $\Lambda$ and $\bar{\Lambda}$. The reconstruction efficiency for $\Lambda$ and $\bar{\Lambda}$ might be improved by using the so-called lambda discs. However, this requires further studies which will be a part of future analysis.

The reconstructed mass for $\Xi\left(1820\right)^{-}$ and $\bar{\Xi}\left(1820\right)^{+}$ is in a good agreement with the literature value [3].

The topology of the decay chain suppresses the background efficiently. The comparison between the number of signal and background events shows how well background events can be suppressed by the selection criteria. After the reconstruction of the full reaction chain, the number of simulated signal events is 8614 and the number of background events is zero. Assuming one single background event gives a limit for the significance of $S > 71.3$. For a more precise statement a more realistic software together with more background simulations is needed.

# References

[1] W. Erni, I. Keshelashvili, B. Krusche, M. Steinacher, Y. Heng, Z. Liu, H. Liu, X. Shen, O. Wang, H. Xu, *et al.*, "Physics performance report for panda: Strong interaction studies with antiprotons," *arXiv preprint arXiv:0903.3905*, 2009.

[2] V. Flaminio, W. G. Moorhead, D. R. O. Morrissson, and N. Rivoire, "Cern report no. cern-hera84-01." (unpublished), 1984.

[3] K. A. Olive *et al.*, "Review of particle physics," *Chin. Phys.*, vol. C38, p. 090001, 2014.

[4] R. Kliemt. private communication, 2015.